Process Modeling and Simulation of the Radiation in the Electric Arc Furnace

authored by T. Meier, K. Gandt, T. Hay, T. Echterhof

and published in *steel research international*

Please cite this article as:

Meier, T.; Gandt, K.; Hay, T.; Echterhof, T.: Process Modeling and Simulation of the Radiation in the Electric Arc Furnace, steel research international, vol. 89 (2018), no. 4, 1700487, DOI: 10.1002/srin.201700487

Link to the original paper:

https://doi.org/10.1002/srin.201700487

Contact

Department for Industrial Furnaces and Heat Engineering
RWTH Aachen University
Kopernikusstr. 10
52074 Aachen, Germany

Website: www.iob.rwth-aachen.de/en/
E-mail: contact@iob.rwth-aachen.de
Phone: +49 241 80 25936
Fax: +49 241 80 22289

Process Modeling and Simulation of the Radiation in the Electric Arc Furnace

Thomas Meier, Karima Gandt, Thomas Hay, Thomas Echterhof*

T. Meier, K. Gandt, T. Hay, Dr.-Ing. T. Echterhof
Rheinisch-Westfälische Technische Hochschule (RWTH) Aachen University,
Department of Industrial Furnaces and Heat Engineering,
Kopernikusstr. 10, 52074 Aachen, Germany
Email: echterhof@iob.rwth-aachen.de

Keywords: electric arc furnace, process modeling, gas radiation, melting geometry, electrode modeling

Abstract

In this paper, an approach to the enhancement of a dynamic process simulation model of an electric arc furnace (EAF) is described by improving the modeling and simulation of the heat transfer especially by radiation within the EAF. The presented work is a continuation of the work of Logar, Dovžan and Škrjanc on modeling the heat and mass transfer and the thermochemistry in an EAF.

The modeling and simulation of the heat transfer within the EAF is improved by including the electrode in the model and considering the convective and radiative heat transfer to and from the electrodes, e.g. by modeling the surface of the electrodes as a radiative surface. Furthermore, the modeling of the melting geometry is improved and implemented in the model in a way to allow for more geometric variability of the scrap meltdown simulation. As a consequence, the view factor calculation within the model is implemented a new way, allowing for a fast and efficient matrix calculation. Finally, the modeling of the thermal radiation of the gas phase is revised to include gas species previously added to the model and to consider emissivity, absorptivity and transmittance of the gas phase as well as the dust load.

1. Introduction

The electric arc furnace (EAF) process is the second most important technique in steelmaking and most significant in scrap recycling. Although the EAF process is highly optimized, the energy and resource efficiency can still be increased. One energy flow not yet used is the off-gas, with which about 20-30% of the total energy input leaves the EAF. Since the off-gas composition and the temperature are continuously measureable, the data can be used to improve the process control. For this purpose, process models have proven their applicability. Furthermore, a detailed understanding of heat and mass transfer during the melting process can be provided.

Logar et al.[1-3] presented a comprehensive deterministic EAF model, which is based on fundamental physical and mathematical equations. Within this model, the main thermal, chemical and mass transfer phenomena in the EAF are calculated with first order ordinary differential equations (ODE). In [4, 5], the model was enhanced by the arc heat distribution and a modified chemical module. The gas phase was designed with a composition of only four components and simplified chemical reactions, since no off-gas data from the furnace used for validation was available. Due to the detailed publication, this model is a suitable basis for further work on gas phase modeling. Therefore, this paper is a continuation of the work of Logar et al.

There are other publications in literature about the modeling of the gas phase in an EAF. However, different approaches and simplifications were made. Matson and Ramirez[6, 7] implemented a gas phase with six chemical elements and equilibrium reactions, which are calculated with a chemical equilibrium algorithm by Gibbs free energy minimization. However, there is no comparison between the simulated results and measured data. Thus, the validity of the model remains questionable. In MacRosty and Swartz[8], all relevant gas phase elements are considered. However, chemical equilibrium is assumed, no gas radiation is implemented and the model requires high computing capacity. The model from Nyssen et al.[9] is insufficiently published to work with it.

Through further separate and joint developments of the model from Logar et al.[1-5], the components H_2, H_2O and CH_4 were included in the gas phase.[10-13] So, all major off-gas components are considered. Furthermore, the chemical reactions were enhanced by three equilibrium reactions and the dissociation of water. In order to keep the simulation times acceptable despite the high complexity of the model, the EAF model was newly implemented in MATLAB to use the internal ODE-solver. To parametrize and validate the model, extensive operational data of an industrial scale 140 t DC-EAF were available. The given data is used as input data for the simulation.

Within this paper, the focus is on the radiation within the gas phase. For this reason, the influence of the added gas phase elements and a different consideration of the electrode are described. The electrode is included in the energy balance and heat transfer mechanisms. Prerequisite for this is the definition of the electrode temperature profile. For increasing the variability, a new melting geometry is developed. Therefore and because of the addition of the electrode, a new view factor definition is necessary. A whole set of view factors for a matrix calculation is defined, because this kind of simulation is fast and efficient. Furthermore, the water input through electrode cooling is added.

The main heat transfer mechanism in the EAF is thermal radiation. Besides the temperature, the most influencing factor on the heat transfer of the gas phase is its composition. Because CO, CO_2, H_2O and CH_4 are selective radiators, the calculation of the thermal radiation was completed and the accuracy of the heat transfer simulation was increased. Therefore, the emissivity, absorptivity and transmittance of the gas phase are implemented.

The presented results are not comparable with measured data because there are no measurements possible. Only an indirect evaluation through comparison of measurable values like gas temperature, gas composition, heat transfer to wall and roof cooling is feasible.

2. Modeling

Within this section, the approach of modeling the electrodes and the gas radiation is described as an enhancement to the dynamic EAF process simulation model from Logar et al.[1, 2] The paper follows the basic assumptions and simplifications as addressed in part 1[1] and part 2[2] of the EAF model publication from Logar et al. The EAF has eight different zones: solid scrap (sSc), slag formers (sSl), liquid melt (lSc), liquid slag (lSl), walls (wall), furnace roof (roof), gas phase (gas) and the electric arc (arc). Each zone and chemical component has assigned physical properties, i.e. specific heat capacity C_p, density ρ and molar Mass M. The values of the used parameters are listed in the Appendix.

2.1. Electrode Zone

In the EAF model according to Logar et al.[2], the graphite electrodes are considered for electrode consumption and are not modeled as an independent zone in the EAF. In addition to the electrode consumption, the water input into the EAF from the spray cooling and the thermal radiation have to be taken into account for the calculation of energy transfer inside the EAF. The arcs between the electrodes and the scrap or melt lead to temperatures of about 3600 K at the tip of the electrode.[14, 15] Thus, the single electrode of a DC-EAF or the three electrodes of an AC-EAF have a significant influence on the energy transfer in the EAF and therefore, the electrodes are implemented as an additional phase with a mass m_{el} and an assumed homogeneous temperature $T_{el\text{-}hom}$ in the EAF model. The differential equation for the change rate of the electrode temperature follows Equation 1:

$$\frac{\mathrm{d}T_{el\text{-}hom}}{\mathrm{d}t} = \frac{\dot{Q}_{el}}{m_{el} C_{p,el}} \qquad (1)$$

In addition to the already implemented electrode consumption as a mass change rate according to Logar et al.[2], additional equations for the calculation of the thermal radiation, the convection and the electrode spray cooling, including the evaporation and the water input into the EAF, are implemented in the model to close the energy balance of the electrode.

In **Figure 1**, the energy balance of a single graphite electrode is shown schematically and the corresponding equation is given in Equation 2:

$$\dot{Q}_{el} = \dot{Q}_{el-rad} + \dot{Q}_{el-conv} - \dot{Q}_{el-cool} + \dot{Q}_{joule} \qquad (2)$$

The supplied electrical power P_{el} is conducted through the electrode to the arc and leads to a heat generation $\dot{Q}_{joule}$. According to Logar et al.[1], this dissipation is assumed as 2.5% of P_{el}.

The heat transfer through radiation $\dot{Q}_{el\text{-}rad}$ and convection $\dot{Q}_{el\text{-}conv}$ can lead to a heat supply as well as heat removal, depending on the temperature difference between electrode and gas phase. $\dot{Q}_{el\text{-}cool}$ is the heat transferred to the cooling water of the electrode spray cooling.

The modeling of the electrodes with a homogeneous temperature is not suitable for the simultaneous description of all heat transfer mechanisms due to the distinctive electrode temperature profile.[14, 15] This temperature profile is caused by the temperature difference between the electrode tip and the spray cooled top. According to the investigations of Rafifei[15] and Guo et al.[14], the electrode is divided into three sections with an abstracted temperature profile. The temperatures of the sections compared to an exemplary temperature profile of the electrode are shown in **Figure 2**.

The average temperatures of the sections are used to calculate the predominantly occurring heat transfer mechanisms in the sections:

- $T_{el\text{-}rad}$ for the heat radiation $\dot{Q}_{el\text{-}rad}$ at the electrode tip,
- $T_{el\text{-}conv}$ for the convection to the EAF gas phase $\dot{Q}_{el\text{-}conv}$ in the middle section and
- $T_{el\text{-}cool}$ for convection at the top end caused by spray cooling.

The temperature $T_{el\text{-}conv}$ differs insignificantly from the homogeneous temperature $T_{el\text{-}hom}$ so that $T_{el\text{-}conv} = T_{el\text{-}hom}$ is defined.

Within the EAF vessel, the convective heat transfer to the gas phase is calculated with Equation 3:

$$\dot{Q}_{el-conv} = \alpha_{el-gas} A_{el} \left(T_{gas} - T_{el\text{-}hom} \right) \tag{3}$$

where $\alpha_{el\text{-}gas}$ is the heat transfer coefficient between the electrode and the gas phase and A_{el} is the surface of the electrode within the EAF vessel, which is dependent on the remaining volume of solid scrap.

A mathematical relationship between the homogeneous electrode temperature $T_{el\text{-}hom}$ and the average temperatures of the defined electrode sections has been derived. The temperatures $T_{el\text{-}rad}$ and $T_{el\text{-}cool}$ are defined by the linear relationships in Equation 4 and 5:

$$T_{el-rad} = K_{el-rad-1}T_{el-hom} + K_{el-rad-2} \tag{4}$$

$$T_{el-cool} = K_{el-cool-1}T_{el-hom} + K_{el-cool-2} \tag{5}$$

where K_{el} are empirical factors and are listed in the Appendix.

The convective heat transfer from the electrode to the cooling water is calculated with Equation 6:

$$\dot{Q}_{el-cool} = \alpha_{el-cool} A_{el-cool} \left(T_{el-cool} - T_{H2O-m}\right)$$

where $\alpha_{el\text{-}cool}$ is the heat transfer coefficient between the electrode and the cooling water, $A_{el\text{-}cool}$ is the wetted surface of the electrode, which is a function of the electrode temperature and $T_{H2O\text{-}m}$ is the average temperature of the water sprayed for cooling. The surface is determined with an approach for evaporation of water at a vertical surface.

The calculation of the heat flow $\dot{Q}_{el\text{-}rad}$ is explained in section 2.4 with the detailed explanation of the thermal radiation.

2.2. Melting Geometry

To determine the thermal radiation between all zones of the EAF, the calculation of view factors, as described in section 2.3, is essential. Therefore, the geometrical dimensions within the EAF are necessary at all times and are calculated with an approximation by a preselected melting geometry. Logar et al.[1] chose a cone frustum with a fixed angle of 45°, which is formed when the arcs between the electrodes and the scrap are boring a hole into the scrap. The fixed angle gives no possibility for variations of the scrap melting geometry, while in reality different charge materials and scrap mixes as well as the operation modes lead to a different melting behavior.

The calculation of the melting geometry is newly implemented to consider different cone angles. Throughout the simulation, the cone angle remains constant. However, by allowing the cone angle to be set by the operator, different scrap mixes and conditions at individual furnaces can be simulated with better accuracy. The selected cone angle determines how fast the electrode will bore down through the scrap and how long the wall will be covered by scrap, which has significant influence on the radiative heat transfer inside the furnace. If available, measurements for electrode position and cooling water temperatures can therefore be used to select the correct cone angle for given circumstances.

With the molten scrap volume $V_{cone\ frustum}$ computed by the simulation, the pre-defined inner cone frustum radius $r_{cone\ in}$ and the chosen angle α, the other cone frustum geometries (cone frustum height h_{cone}, outer cone frustum radius $r_{cone\ out}$ and the free wall height) can be determined by means of a zero-point calculation solving by Equation 7:

$$V_{cone\ frustum} = \frac{\pi h}{3}\left(R^2 + Rr + r^2\right) = \frac{\pi h_{cone}}{3}\left(r_{cone\,out}^2 + r_{cone\ out} r_{cone\ in} + r_{cone\ in}^2\right) \qquad (7)$$

where h_{cone} is the height and r are the radii of the cone frustum. A figure of the dimensions is given in Logar et al.[1] The calculation is time-consuming because there is no closed solution for the cubic equation for the cone frustum volume.

Therefore, the geometric dimensions during the melting process are pre-calculated as a function of the remaining solid scrap volume and are transferred to the simulation as an interpolation function $f(V_{sSc})$ to eliminate the need of a time-consuming zero-point calculation during the simulation.

The calculation of the geometric dimensions of the cone frustum is performed with a rotation volume around the vertical axis of the assumed cylindrical EAF vessel. For this purpose, the EAF geometry is shown in **Figure 3 a**. The geometrical dimensions still correspond to the definition from Logar et al.[1] In addition, the angle α is definable, which determines the steepness of the cone frustum respectively the borehole in the scrap.

The calculation of the volume of the melted scrap corresponds to the described cone frustum and is determined by a volume calculation of a rotary body according to Equation 8:

$$V_{cone\ frustum} = \pi \int_{y_1}^{y_2} \left[f^{-1}(y) \right]^2 dy \tag{8}$$

where *f* is the function of the surface line of the melting cone, which is integrated within the boundaries y_1 to y_2. Together with the function *f*, the boundaries describe the positions of $r_{cone\ in}$ and $r_{cone\ out}$ according to Equation 9.

$$y_2 = f_i\left(x = r_{EAF\ out}\right) \text{for } f_i^{-1}\left(y = h_{sSc,0}\right) \geq r_{EAF\ out} \tag{9}$$

Figure 3 b shows the boundaries for integration depending on the remaining scrap volume throughout the simulation.

2.3. View Factors

With the electrode considered in the EAF model, the calculation of the thermal radiation and especially the view factor calculation have been enhanced. Therefore, the view factors are calculated for the six surfaces *k* inside the EAF to obtain a complete 6x6 matrix. The subsequent calculation of the thermal radiation of all surfaces is thus simplified by means of a matrix operation.

The arrangement of the surfaces within the EAF is illustrated in **Figure 4**. Because of the roof heart for the electrodes, the roof (1) is assumed to be a circular ring. The water-cooled walls (2) correspond to the lateral surface of a cylinder, which has an increasing cylinder height with decreasing scrap height. The solid scrap (3) is assumed to be a homogeneous surface. Because of the melting process, it forms a cone frustum, which is composed of the partial surfaces (circular ring of remaining solid scrap (3-1), lateral of cone frustum (3-2), circular surface at the bottom of the cone frustum (3-3) and at the top (3-4)). The surfaces of the arc (5), here assumed to be cylindrical, and the electrodes (6) complete the geometry of the approximated EAF.

Compared to the implementation according to Logar et al.[1, 3], the view factors VF_{22}, VF_{33}, VF_{34}, VF_{43} as well as all the view factors VF_{i6} and VF_{6j} associated with the electrode surface are calculated in the EAF model to complete the view factor matrix in Equation 10:

$$VF = \begin{bmatrix} VF_{11} & VF_{12} & VF_{13} & VF_{14} & VF_{15} & VF_{16} \\ VF_{21} & VF_{22} & VF_{23} & VF_{24} & VF_{25} & VF_{26} \\ VF_{31} & VF_{32} & VF_{33} & VF_{34} & VF_{35} & VF_{36} \\ VF_{41} & VF_{42} & VF_{43} & VF_{44} & VF_{45} & VF_{46} \\ VF_{51} & VF_{52} & VF_{53} & VF_{54} & VF_{55} & VF_{56} \\ VF_{61} & VF_{62} & VF_{63} & VF_{64} & VF_{65} & VF_{66} \end{bmatrix} \tag{10}$$

View factors of the electrode VF_{i6} and VF_{6j}

In the case of an AC-EAF, the three electrodes are combined into one substitute electrode with the same surface as the three individual electrodes. The only exception is VF_{66}, which is the view factor of the electrodes to themselves, which is calculated with Equation 11:[16]

$$VF_{66} = \begin{cases} \dfrac{1}{\pi}\left(\sqrt{\left(\dfrac{h_{el}}{r_{el}}\right)^2 - 4} - \dfrac{h_{el}}{r_{el}} + 2\arcsin\dfrac{2r_{el}}{h_{el}} \right) & \text{for AC-EAF} \\ 0 & \text{for DC-EAF} \end{cases} \tag{11}$$

The view factors of the electrode to the roof VF_{61}, to the walls VF_{62} and to the melt VF_{64} are compared with VF_{51} and VF_{52} with the geometrical dimensions of the electrode as described in Logar et al.[1, 3]

It is assumed that the heat transfer from the arc to the electrode is already part of the heat flow $\dot{Q}_{joule}$ in section 2.1. and can be accounted for by correcting the ratio of electric power input that is dissipated. While radiative heat exchange between arc and electrode tip change, the surface area of the electrode that is directly irradiated by the arc is comparatively small and the geometric conditions around the between the arc and the electrode tip remain similar throughout the process. It is assumed that the error stemming from this simplification is insignificant for the overall simulation result. The direct heating of the electrode tip with its correspondingly increased temperature compared to the average electrode temperature is accounted for through the temperature profile as given in Figure 2.Therefore, the view factors between the arc and electrodes VF_{65} and VF_{56} are neglected and set to $VF_{65} = VF_{56} = 0$. Finally, the view factor VF_{63} is calculated with the summation rule in Equation 12:

$$\sum_{i=1}^{6} VF_{6i} = 1 \tag{12}$$

and the reciprocal view factors VF_{i6} of the electrode are determined with the reciprocity theorem in Equation 13:

$$A_6 VF_{6i} = A_i VF_{i6} \tag{13}$$

Remaining view factors VF_{22}, VF_{33}, VF_{34} and $VF43$

The view factor VF_{22} of the wall to itself is calculated with an approximation equation for the inner surface of a cylinder with a coaxial cylinder on the symmetry axis with Equation 14, 15 and 16:[16, 17]

$$VF_{22} = \frac{1}{\pi R_2}\left[\pi\left(R_2 - R_1\right) + \cos^{-1}\left(\frac{R_1}{R_2}\right) - \sqrt{1+4R_2^2}\,\tan^{-1}\left(\frac{\sqrt{\left(1+4R_2^2\right)\left(R_2^2 - R_1^2\right)}}{R_1}\right) + 2R_1\tan^{-1}\left(2\sqrt{R_2^2 - R_1^2}\right)\right] \tag{14}$$

with

$$R_1 = \frac{r_{el}}{h_{wall}} \tag{15}$$

$$R_2 = \frac{r_{EAF\,out}}{h_{wall}} \tag{16}$$

The view factor VF_{33} is calculated with the summation rule analogously to Equation 12. The view factor VF_{43} is obtained by applying the summation rule analogously in Equation 12 and with the reciprocity theorem, VF_{34} follows analogously with Equation 13.

2.4. Thermal Radiation

Thermal radiation is one of the main heat transfer phenomena in the EAF. With the enhancement of the gas phase by further elements, the gas radiation is no longer negligible as H_2O, CO, CO_2 and CH_4 are effective radiators.[11, 12] Therefore, the emissivity and absorptivity of the gas components are calculated dependent on the actual gas composition and gas temperature with an assumed equal layer thickness, which is described in the following section. In order to boost the efficiency of the calculation of the thermal radiation, it is implemented via matrix operations according to Equation 17:

$$\vec{\dot{Q}}_{rad} = diag\left(\vec{A}\right)\left(\vec{J} - \vec{G}\right) \tag{17}$$

where $\vec{\dot{Q}}_{rad}$ is the heat radiation vector for each of the six surfaces, $\vec{A}$ is the surface vector, $\vec{J}$ is the radiosity vector and $\vec{G}$ is the irradiation vector for each surface. The numbers of the surfaces described in the view factor description are representing the positions in the vectors. For a detailed understanding of the thermal radiation inside the EAF, **Figure 5** schematically represents the thermal radiation exchange at an EAF surface.

The realization of the matrices calculation requires the calculation of all view factors VF_{ij} in the EAF including the electrode without simplifying or neglecting any surface to obtain the 6x6 matrix as described before. With that, the irradiation G is obtained by Equation 18 for a single surface and Equation 19 for the matrices operation:

$$G_i = \sum_{j=1}^{n} [\tau_{gas-j} J_j + \varepsilon_{gas} \sigma T_{gas}^4] VF_{ij} = E_{gas} + \sum_{j=1}^{n} \tau_{gas-j} J_j VF_{ij} \tag{18}$$

$$\vec{G} = VF\left[diag\left(\vec{J}\right)\vec{\tau}_{gas}\right] + \begin{pmatrix} 1 \\ \vdots \\ 1 \end{pmatrix} \varepsilon_{gas} \sigma T_{gas}^4 \tag{19}$$

where τ_{gas} are the transmittances of the gas phase for each surface, ε_{gas} is the emissivity of the gas, σ is the Stefan Boltzmann constant and E_{gas} is the emission of the gas phase, which is calculated by the second summand in Equation 19.

The radiosity *J* is determined by Equation 20 for each surface *i* or with Equation 21 for all surfaces with *M* being a matrix calculated according to Equation 22:

$$J_i = E_i + (1-\varepsilon_i) E_{gas} + (1-\varepsilon_i) \sum_{j=1}^{n} \tau_{gas-j} J_j VF_{ij} \tag{20}$$

$$\vec{J} = M^{-1} \left(\vec{E} + \left(\begin{matrix} 1 \\ \vdots \\ 1 \end{matrix} - \vec{\varepsilon} \right) E_{gas} \right) \tag{21}$$

$$M = \begin{bmatrix} \tau_{gas-1}(\varepsilon_1 - 1) VF_{11} + 1 & \cdots & \cdots & \tau_{gas-6}(\varepsilon_1 - 1) VF_{16} \\ \vdots & \tau_{gas-2}(\varepsilon_2 - 1) VF_{22} + 1 & & \vdots \\ \vdots & \vdots & \ddots & \vdots \\ \tau_{gas-1}(\varepsilon_6 - 1) VF_{61} & \cdots & \cdots & \tau_{gas-6}(\varepsilon_6 - 1) VF_{66} + 1 \end{bmatrix} \tag{22}$$

The emission E_i for each surface *i* is determined with Equation 23:

$$E_i = \varepsilon_i \sigma T_i^4 \tag{23}$$

where ε_i are the emissivities of the corresponding surfaces, which are chosen according to Logar et al.[1]

Finally, the thermal radiation of the gas phase $\dot{Q}_{gas\text{-}rad}$ is calculated with an energy balance according to Equation 24:

$$\dot{Q}_{gas-rad} = \sum_{i=1}^{n} \left[A_i \left(E_{gas} - \sum_{j=1}^{n} \alpha_{gas-j} J_j VF_{ij} \right) \right] \tag{24}$$

2.5. Emissivity, absorptivity and transmittance of the gas phase

The off-gas components CO, CO_2, CH_4 and H_2O are effective emitters. They emit and absorb radiation energy in spectral bands. In addition to the gases, the dust in the EAF gas contributes significantly to the heat radiation. According to Brummel[18], the total emissivity ε_{gas} of the gas phase is calculated by Equation 25:

$$\varepsilon_{gas} = \varepsilon_{gas-sum} + \varepsilon_{dust} - \varepsilon_{gas-sum} \varepsilon_{dust} \tag{25}$$

where $\varepsilon_{gas\text{-}sum}$ is the emissivity of the gas phase caused by the off-gas components CO, CO_2, CH_4 and H_2O and ε_{dust} is the emissivity of the gas phase caused by the dust load.

Emissivity ε_{dust}

The average dust load for the whole process is assumed to be between 30 and 50 g m^{-3} (constant particle diameter of d_p = 500 µm) and depends on the scrap height.[19] It is assumed that the average dust load is highest after the charging of scrap and decreases with increasing melting time. The emissivity is then calculated according to Brummel.[18]

Emissivity $\varepsilon_{gas\text{-}sum}$

$\varepsilon_{gas\text{-}sum}$ is the emissivity of the gas phase caused by the off-gas components CO, CO_2, CH_4 and H_2O. All four are selective emitters. Since the emission bands of H_2O and CO_2 are interfering, a common emissivity must be specified. Hofer[20] determines the total emissivity of the gas phase $\varepsilon_{gas\text{-}sum}$ as a function of the individual emissivities ε_i using Equation 26 according to Vortmeyer[21]:

$$\varepsilon_{gas-sum} = \varepsilon_{H2O+CO2} + \varepsilon_{CH4} + \varepsilon_{CO} \tag{26}$$

The emissivity $\varepsilon_{H2O+CO2}$ consists of the individual emissivities ε_{H2O} and ε_{CO2} and is determined by Equation 27:[22]

$$\varepsilon_{H2O+CO2} = \left(\varepsilon_{H2O} + \varepsilon_{CO2}\right) K_{\varepsilon-H2O+CO2} \tag{27}$$

where $K_{\varepsilon\text{-}H2O+CO2}$ is a correction factor, which is a function of the partial pressures p_i and an equivalent layer thickness s_{eq} and is calculated by Equation 28:[22]

$$\begin{aligned} K_{\varepsilon-H2O+CO2} &= f\left(s_{eq}\, p_i\right) \\ &= 1 + \frac{0.25 s_{eq}\left(p_{H2O} + p_{CO2}\right)}{0.11 + s_{eq}\left(p_{H2O} + p_{CO2}\right)} \left(1 - \frac{p_{CO2}}{p_{H2O} + p_{CO2}}\right) \ln\left(1 - \frac{p_{CO2}}{p_{H2O} + p_{CO2}}\right) \end{aligned} \tag{28}$$

The emissivities ε_{H2O} and ε_{CO2} are calculated as a function of their partial pressures p_i, the gas temperature T_{gas} and the equivalent layer thickness s_{eq}, shown in Equation 29 and 30:[22]

$$\varepsilon_{H2O} = f\left(T_{gas}, p_{H2O}s_{eq}\right) = \left(K_{\varepsilon-H2O-1} - K_{\varepsilon-H2O-2}T_{gas}\right)\left(1-\exp\left(-K_{\varepsilon-H2O-3}K_{\varepsilon-H2O-4}\right)\right) \tag{29}$$

$$\varepsilon_{CO2} = f\left(T_{gas}, p_{CO2}s_{eq}\right) = K_{\varepsilon-CO2-1} + K_{\varepsilon-CO2-2}\gamma + K_{\varepsilon-CO2-3}\gamma^2 + K_{\varepsilon-CO2-4}\gamma^3 \tag{30}$$

where $K_{\varepsilon\text{-}i\text{-}j}$ and γ are empirical factors which can be taken from Vortmeyer and Kabelac[22]. The validity of these experimentally determined analytical equations is limited to a narrow layer thickness range as well as limited pressure and temperature ranges. Because of the absence of an alternative, especially a manageable approach, and the model simplification of a homogeneous gas phase, the equations are applied and have already delivered useful results at Hofer[20] for off-gas modeling in the dedusting system.

The equivalent layer thickness s_{eq} is the ratio of the gas volume V_{gas} and the limiting surface area. s_{eq} represents the radius of a hemisphere, which has the same emission capacity as the actual body. As a sufficient and established approximation, Equation 31 applies:[22]

$$s_{eq} = 0.9\frac{4V}{A} = 0.9\frac{2r_{EAF\,out}}{1+\frac{r_{EAF\,out}}{h_{EAF\,up}}} \tag{31}$$

The emissivities of CO and CH_4 are not determined with analytical approximations, but with a two-dimensional interpolation of experimental values, in which the emissivities are given as a function of the partial pressure and the temperature. The diagram for CO is from Beer at al.[23] and for CH_4 from Vortmeyer and Kabelac.[22]

Absorptivities

Analogously to the gas phase emissivity ε_{gas}, the gas phase absorptivity α_{gas} is determined. In contrast to the emissivitities, the absorptivities are determined as a function of the surrounding surface temperatures T_k. Thus, six absorptivities of the corresponding surrounding surfaces j are calculated with Equation 32[18] and 33[21] according to [20]:

$$\alpha_{gas,j} = \alpha_{gas-sum,j} + \varepsilon_{dust} - \alpha_{gas-sum,j}\varepsilon_{dust} \tag{32}$$

$$\alpha_{gas-sum,j} = \alpha_{H2O+CO2,j} + \alpha_{CH4,j} + \alpha_{CO,j} \tag{33}$$

The absorptivity $\alpha_{H2O+CO2}$ is determined with the individual emissivities α_{H2O} and α_{CO2} with Equation 34:[22]

$$\alpha_{H2O+CO2,j} = \left(\alpha_{H2O,j} + \alpha_{CO2,j}\right) K_{\alpha-H2O+CO2,j} \tag{34}$$

where $K_{\alpha\text{-}H2O+CO2}$ is a correction factor, which is calculated by Eq. (27) but with adapted partial pressures $p_{i\text{-}\alpha}$ calculated with Equation 35:

$$p_{i-\alpha,k} = p_i \frac{T_{surf,j}}{T_{gas}} \tag{35}$$

Assuming a total pressure of about 1 bar, the absorptivities for H_2O and CO_2 are calculated as a function of the temperature of the surface j $T_{surf,j}$ with Equation 36 and 37:[22]

$$\alpha_{H2O,j} = \varepsilon_{H2O-\alpha} \left(\frac{T_{surf,j}}{T_{gas}}\right)^{0.45} \tag{36}$$

$$\alpha_{CO2,j} = \varepsilon_{CO2-\alpha} \left(\frac{T_{surf,j}}{T_{gas}}\right)^{0.65} \tag{37}$$

where $\varepsilon_{H2O\text{-}\alpha}$ and $\varepsilon_{CO2\text{-}\alpha}$ are adapted emissivities, which are determined with Equation 29 and 30 for the temperature $T_{surf,j}$ instead of T_{gas}, and the adapted partial pressures according to Equation 35.

There are no equations to convert the emissivities of CH_4 and CO to their absorptivities, so that these are calculated according to the interpolation for their emissivities. The partial pressure is calculated with Equation 35 and for the temperature, the corresponding surface temperature $T_{surf,j}$ is used.

Transmittance

The transmittance of the gas phase τ_{gas} is calculated with Equation 38:

$$1 = \alpha_{gas,j} + \tau_{gas} + \rho_{gas} \tag{38}$$

where ρ_{gas} is the reflectance of the gas phase, which is set to $\rho_{gas} = 0$.

2.6. Influence of foaming slag height

Foaming slag is used in the EAF process to shield the arcs and melt and thereby reduce radiation on the refractory lining and cooled wall and roof sections of the EAF. This reduces thermal losses and refractory wear, making the process more efficient[19].

In the presented model the height of the foaming slag is estimated based on the approach proposed by Logar et al. [2] with the slag index according to MacRosty et al.[8]. In the current model the temperature of the liquid slag zone which would emit radiation while it covers the melt remains close (within 15 K) to that of the bath. Therefore, any influence of slag on the radiation from the bath is neglected in the current model. The covering of the arc by foaming slag on the other hand has significant influence on the energy radiated onto different surfaces. This influence is modeled by adjusting the ratio of arc power radiated $P_{arc\text{-}melt}$. Depending on the ratio of slag height H_{slag} to arc length H_{arc}, less energy is emitted by radiation while the share of arc power used for direct heating of the melt $P_{arc\text{-}melt}$ is increased as shown in Equation 39-40. $K_{slag\text{-}influence}$ is an empirical factor determining how much the power distribution is adjusted with changing slag heights, $K_{arc\text{-}radiation}$ and $K_{arc\text{-}lSc}$ represent the empirical distribution of arc power into radiation and direct melt heating.

$$K_{slag} = K_{slag-\inf luence} \max(\frac{H_{slag}}{H_{arc}},1) \tag{38}$$

$$P_{arc\_radiation} = P_{arc} K_{arc-radiation} (1 - K_{slag}) \tag{39}$$

$$P_{arc-lSc} = P_{arc} (K_{arc-radiation} K_{slag} + K_{arc-lSc}) \tag{40}$$

3. Results and Discussion

Within this section, the results of the investigations are presented. The results of the simulation can not be compared to data from measurements like temperatures, heat flows, etc. as those are not available. However, the results show the influence of the implemented mechanisms.

The simulation is parametrized for an industrial scale DC-EAF with a 140 t tapping weight. The input data for scrap and the operational data for power and mass flows into the EAF were provided. The operational data is available with a resolution of five seconds and is evaluated with an interpolation approach for each integration time step to determine the input mass flows and powers. In total, 126 heats were simulated and evaluated in terms of the temperature profile and heat transfers of the electrode, selected view factors and the radiation heat flow with the emissivity and selected absorptivity of the gas phase. The hot heel was set to 30 t. Table 1 and 2 show model parameters and factors used in the simulation. The process simulation was performed with MATLAB R2015b on a PC with 3.4 GHz, 16 GB RAM and Windows 7 64 bit. The relative integration tolerance was set to 10^{-9}. The simulation time was in the range of 65 s to 85 s for one heat. Despite the high model complexity, these short simulation times are possible since the simulation is accelerated with ODE-solver after the model enhancements. By using the possibility of parallel computing, the 126 heats are simulated on four processor cores in less than one hour. Therefore, the model is applicable for online process optimization.

Figure 6 shows the different temperatures of the electrode for the calculation of heat transfer through water cooling, convection and radiation. As described in section 2.1, the electrode is divided into three sections dependent on the dominated heat transfer. The homogenous temperature $T_{el\text{-}hom}$ is temperature for the calculation of the convection heat transfer to the EAF gas phase $\dot{Q}_{el\text{-}conv}$, which dominates in the middle section of the electrode. The temperatures $T_{el\text{-}rad}$ at the electrode tip and $T_{el\text{-}cool}$ at the top caused by spray cooling are calculated with approximation in Eq. (4). In the beginning of the batch, the temperatures decrease because the electrode is surrounded by cold scrap. As a result of charging the second basket, the temperatures drop at 30% of process time. There is a further fall of temperature at the end of the heat since the electrical power is switched off for the manual measurement of the melt temperature.

In **Figure 7**, the energy balance of the electrode according to Equation 2 is illustrated. The dissipation $\dot{Q}_{joule}$ is not shown, as it is not dependent on the electrode temperatures. The values of the partial heat flows are within the range from -2.2 MW to 0.5 MW. The net electrode heat flow $\dot{Q}_{el}$ differs from almost -3 MW to 2 MW. The water input for electrode cooling presently is implemented with a constant mass flow of about 30 l min^{-1} as this this describes the current procedure in industry. To optimize the energy efficiency of the EAF process, the model can be used to adapt the water input of the electrode. An adjusted reduction of cooling water would have the further advantage that less water is introduced into the furnace. $\dot{Q}_{el}$ declines in the negative half in a few points because of moments of power off. The first drop is due to arc instabilities directly after charging the first basket. After 30% of the process time, the second basket is charged. At the end of the heat, the temperature of the melt is measured.

The geometrical conditions in the EAF are shown in **Figure 8**. The height of the cone frustum h_{cone}, which is formed during the melting of the scrap through the arc, and the height of the solid scrap h_{scrap} have a repetitive similar course: When scrap has been loaded into the furnace through a basket (at 0% and 25% of the process time), the scrap height is at its maximum. The cone frustum is formed by boring of the arc, which is represented by the steep increase of h_{cone}. Afterwards, the cone frustum and the scrap height slightly decrease. The arc is connected with the liquid bath and melts the scrap by increasing the cone frustum radii. Then, the remaining scrap, which is stacked next the walls, is melted. The cone frustum and the scrap height fall to zero, since only the liquid melt is in the furnace.

The height of the free wall h_{wall} an opposed course. This height relevant for thermal radiation load on the cooling water within the walls. This fact is taken into account by the view factor between the electrode (6) and the wall (2) VF_{62}, which is shown in **Figure 9**. Furthermore, the view factors from the electrode (6) to the roof (1) VF_{61} and to the melt (4) VF_{64} are illustrated.

The view factor between the electrode (6) and the wall (2) VF_{62} has a similar course like the free wall height h_{wall}. If the wall is covered by scrap, limited electrode radiation is transferred. The electrode-roof view factor VF_{61} remains almost constant since the mutual geometrical viewing conditions are not disturbed by the scrap. The view factor between electrode (6) and the melt (4) VF_{64} depends on the area covered by scrap at the beginning of the heat and after charging of the second basket.

In **Figure 10**, the view factors from the melt (4) VF_{43}, the arc (5) VF_{53} and the electrode (6) VF_{63} to the scrap (3) are shown. These view factors decrease with reducing solid scrap volume V_{sSc} and are zero when no scrap is left.

Directly after charging, the melt is covered by scrap. There is no radiation transfer between the phases, but thermal conduction. Therefore, the view factor from the melt (4) to the scrap (3) VF_{43} increase, when the arc bores the cone frustum and the melt's surface appears. High values of the view factor between the arc (5) and the scrap (3) VF_{53} means high efficiency of the melting process. The arc is attached to the solid scrap and the heat radiation transfer is high.

The simulated results for the total gas radiation $\dot{Q}_{gas\text{-}rad}$ and the gas emissivity ε_{gas} are shown in **Figure 11**. A positive value of $\dot{Q}_{gas\text{-}rad}$ means that the gas phase receives energy. Since this is most of the time the case, the gas phase has a significant influence on the energy efficiency of the EAF process. In addition, this underlines the importance of the gas phase within the simulation of the energy distribution inside the EAF. The total gas radiation $\dot{Q}_{gas\text{-}rad}$ is negative during power-off times while charging and measurements.

In Meier et al.[11], the results of the simulation results of the energy and mass transfers in combination with a model of the dedusting system are presented. In particular, the composition and temperature of the gas phase are pointed out. After charging, the amounts of H_2 and CO are high, which leads according to Equation 26, 27 and 28 to a maximum value of the gas emissivity ε_{gas}.

Last but not least, the results for the gas absorptivities for the neighboring surfaces roof $\alpha_{gas\text{-}roof}$, wall $\alpha_{gas\text{-}wall}$, melt $\alpha_{gas\text{-}lSc}$ and solid scrap $\alpha_{gas\text{-}sSc}$ are shown in **Figure 12**. Up to half the tap-to-tap time t_{tap}, the absorptivities $\alpha_{gas\text{-}roof}$, $\alpha_{gas\text{-}wall}$ and $\alpha_{gas\text{-}sSc}$ are in the same range, with $\alpha_{gas\text{-}sSc}$ being slightly higher, since the scrap temperature is in the range that gives the highest gas absorptivity while the melt is hotter and roof and wall surfaces are cooler. Later in the process the scrap temperature increases further with the absorptivity decreasing accordingly, while the roof and wall temperatures as well as the respective absorptivities increase.

The steep changes in absorptivity that can be seen in $\alpha_{gas\text{-}roof}$ at around 90% of the process time and occur in the other absorptivites at various times as well are due to the limited available data for the emissivity of CO. Below 550 K the approximation used in the model assumes the absorptivity to be zero, with a comparatively steep increase for temperatures just above this value. The impact of these sudden changes in absorptivity over certain surfaces on the overall simulation results is negligible.

While direct validation of the calculated radiative heat transfer inside the furnace is not possible since it cannot be measured, indirect validation through measurements for example of cooling water temperatures and the spot measurements of the bath temperature is feasible. **Figures 13** and **14** show examples for the measured and simulated outlet temperatures for the roof and wall cooling. Radiation has a strong influence on these values and the calculated results are in good agreement with the measured data except for the simulated wall temperature exceeding the measured values during the final part of the process. Radiation represents the main heat flux into the wall at this time and there are several reasons why it might be too high. These include lack of data for the exact geometry of the furnace, the data was obtained from, as well as too high overall energy release in the simulation, which could be due to inaccuracies in the chemical model and unknown composition of charged material.

Figure 15 shows an example of the simulated bath temperature with three measurements taken during the process. The steel temperature strongly depends on other modules, especially the chemistry and corresponding energy release, but radiation is a significant influence. The temperature rises faster than the measurements show, for reasons similar to those leading to the high wall cooling water temperature. **Figure 16** shows the gas temperature. The equipment used cannot measure values lower than 1000 °C, so while the simulated results start at a much lower temperature the measured values only become relevant when they exceed 1000 °C. The calculated results are lower than the measured values after charging but in good agreement during the later stages of the process. Because of the low mass and heat capacity of the gas zone the occurring differences in temperature still only represent a comparatively small fraction of the total energy content of the furnace at any given time.

4. Conclusion

Within this paper, parts of the enhancements of the re-implemented and already further developed[10-13] model from Logar et al.[1-5] are presented. The calculation of the radiation within the EAF is described. First, the electrode was included as surface part of the heat transfers within the EAF. For this purpose, the electrode was divided into three areas, in which a certain heat transfer mechanism dominates: convection at the top caused by the water spray cooling, heat transfer to the gas phase by convection in the middle and radiation at the electrode tip due to the high temperature caused by the arc. The according temperatures were determined, the separate heat flows calculated and finally, the net electrode heat flow could be simulated. Second, a new melting geometry was developed. In comparison to Logar et al.[3], the melting geometry was implemented with more variability. Furthermore, the surface of the electrode was modelled as a radiative surface. However, this meant the new implementation of the view factors, which are now determined in a fast and efficient matrix calculation. Third, the composition of the gas phase was expanded by the selective radiators CO, CO_2, H_2O and CH_4. The emissivity, absorptivity and transmittance of the gas phase is calculated differently and the dust load is considered. Finally, the thermal radiation of the gas phase within the EAF is simulated. In order to keep the simulation time short despite the high model complexity, the ODE solver ode15s for stiff ODE systems was used.

Within the result section, the simulated values of the electrode temperatures and the electrode heat flows are presented. The results of the melting geometry and selected view factors are described. The profile of the total gas radiation, the gas emissivity and the gas absorptivities for the roof, the wall, the melt and the solid scrap are illustrated and discussed. For the simulation, the operational data of 126 heats from a 140 t DC-EAF were used. It is not technically possible to measure the simulated data and to validate the model in point of radiation. Only an indirect evaluation through comparison of measurable values like gas temperature, gas composition, heat transfer to wall and roof cooling is feasible.

There is potential for further optimization in the calculation of the radiative heat transfer. Testing with the current model has indicated that the calculated heat flow to the wall and the resulting cooling water temperatures are too high in comparison with available measurements. This potentially stems from simplifications in the model geometry that disregards that the cooling panels forming the wall do not necessarily begin right above the bottom vessel. Preliminary testing indicates that including this segment in the geometry and view factor calculations (leading to a 7x7 view factor matrix) may give more accurate results for the radiative heat transfer. Additionally better understanding of dust production and the resulting dust loading of the gas could lead to better results for the emissivity of the gas during the process.

Since the simulation takes less than one minute per heat, the model is applicable for online optimization. With parallel computing, it is possible to simulate hundreds of different setting, input material or operation strategies within an acceptable time. Therefore, the model offers the possibility to train operators or to carry out offline investigations on the efficiency increase. The model also offers better understanding of the process through the calculation and visualization of heat flows inside the furnace that currently cannot be measured.

References

[1] V. Logar, D. Dovzan, I. Skrjanc, *ISIJ Int.* **2012**, *52*, 402.

[2] V. Logar, D. Dovzan, I. Skrjanc, *ISIJ Int.* **2012**, *52*, 413.

[3] V. Logar, I. Skrjanc, *ISIJ Int.* **2012**, *52*, 1224.

[4] A. Fathi, Y. Saboohi, I. Skrjanc, V. Logar, *Steel Res. Int.* **2017**, *88*, 1600083.

[5] A. Fathi, Y. Saboohi, I. Skrjanc, V. Logar, *ISIJ Int.* **2015**, *55*, 1353.

[6] S. A. Matson, W. F. Ramirez, 55th Electr. Furn. Conf., Chicago, IL, USA **1997**, 675.

[7] S. A. Matson, W. F. Ramirez, P. Safe, 56th Electr. Furn. Conf., 16th Process Technol. Conf., New Orleans, LA, USA, **1998**.

[8] R. D. M. MacRosty, C. L. E. Swartz, *Ind. Eng. Chem. Res.* **2005**, *44*, 8067.

[9] P. Nyssen, G. Monfort, J.L. Junque, M. Brimmeyer, P. Hubsch, J.C. Baumert, 2nd Int. Conf. Model. Simul. Metall. Processes Steelmak. (SteelSim), Graz/Seggau, Austria, **2007**, 33.

[10] T. Meier, K. Gandt, T. Echterhof, H. Pfeifer, *Metall. Mat. Trans. B*, DOI:10.1007/s11663-017-1093-7.

[11] T. Meier, A. Hassannia Kolagar, T. Echterhof, H. Pfeifer, Proc. of 11th Eur. Electr. Steelmak. Conf. (EEC), Venedig, Italy, **2016**, 1-10.

[12] T. Meier, A. Hassannia Kolagar, T. Echterhof, H. Pfeifer, Proc. of 6th Int. Conf. Model. Simul. Metall. Process Steelmak. (SteelSim), Bardolino, Italy, **2015**.

[13] T. Meier, V. Logar, T. Echterhof, I. Skrjanc, H. Pfeifer, *Steel Res. Int.* **2015**, *87*, 581.

[14] D. Guo, G. A. Irons, Iron Steel Technol. Conf., AISTech, Nashville, TE, USA, **2004**, 991.

[15] R. Rafiei, A. Kermanpur, F. Ashrafizadeh, *Ironmak. Steelmak.* **2008**, *35*, 465.

[16] J. R. Howell, A catalog of radiation heat transfer configuration factors, http://www.thermalradiation.net/indexCat.html, accessed: December 2015.

[17] D. C. Hamilton, W. R. Morgen, *NACA technical note TN-2836*, NACA, Washington D.C., **1952**.

[18] H.-G. Brummel, *VDI-Wärmeatlas*, 11. ed., Springer, Berlin, Germany **2013**, 1129.

[19] Y. N. Toulouevski, I. Y. Zinurov, *Innovation in electric arc furnaces. Scientific basis for selection*, Springer, Heidelberg, Germany, **2010**.

[20] M. Hofer, *Dissertation*, TU Wien, **1997**.

[21] D. Vortmeyer, *VDI-Waermeatlas*, 7. ed., Springer, Berlin, Germany, **1994**, 523.

[22] D. Vortmeyer, S. Kabelac, *VDI-Wärmeatlas*, 11. ed., Springer, Berlin, Germany **2013**, 1115.

[23] J. M. Beer, P. J. Foster, R. G. Siddall, *Calculation Methods of Radiative Heat Transfer*, Heat Transfer and Fluid Flow Service (HTFS) at the Harwell Laboratory, England, **1971**.

Appendix

List of symbols

Greek letters

α	Angle for melting geometry
α_i	Absorptivity of the surface *i*
$\alpha_{CH4,j}$	Absorptivity of the gas phase caused by CH_4 for the surface *j*
$\alpha_{CO,j}$	Absorptivity of the gas phase caused by CO for the surface *j*
$\alpha_{gas\text{-}i}$	Absorptivity of the gas phase for the surface *j* for the surface *j*
$\alpha_{gas\text{-}sum,j}$	Absorptivity of the gas phase caused by the elements CO, CO_2, CH_4 and H_2O for the surface *j*
$\alpha_{CO2,j}$	Absorptivity of the gas phase caused by CO_2 for the surface *j*
$\alpha_{H2O,j}$	Absorptivity of the gas phase caused by H_2O for the surface *j*
$\alpha_{H2O+CO2,j}$	Absorptivity of the gas phase caused by H_2O and CO_2 for the surface *j*
$\alpha_{el\text{-}gas}$	Heat transfer coefficient between the electrode and the gas phase
$\alpha_{el\text{-}cool}$	Heat transfer coefficient between the electrode and the spray cooling water
γ	Empirical factor for the calculation of ε_{CO2}
ε_{dust}	Emissivity of the gas phase caused by the dust load
ε_{CH4}	Emissivity of the gas phase caused by CH_4
ε_{CO}	Emissivity of the gas phase caused by CO
ε_{CO2}	Emissivity of the gas phase caused by CO_2
$\varepsilon_{CO2\text{-}\alpha}$	Emissivity of the gas phase caused by CO_2 used for the calculation of the absorptivity $\alpha_{CO2,j}$ for the surface *j*
ε_{gas}	Emissivity of the gas phase
$\varepsilon_{gas\text{-}sum}$	Emissivity of the gas phase caused by the elements CO, CO_2, CH_4 and H_2O
ε_{H2O}	Emissivity of the gas phase caused by H_2O

$\varepsilon_{H2O\text{-}\alpha}$	Emissivity of the gas phase caused by H_2O used for the calculation of the absorptivity $\alpha_{H2O,j}$ for the surface j
$\varepsilon_{H2O+CO2}$	Emissivity of the gas phase caused by H_2O and CO_2
ε_i	Emissivity of the surface i
$\vec{\varepsilon}$	Emissivity vector for each of the six surfaces
π	Pi
ρ	Density
ρ	Reflectance
σ	Stefan Boltzmann Constant
$\tau_{gas\text{-}j}$	Transmittance of the gas phase for the surface j
$\vec{\tau}_{gas}$	Transmittance vector of the gas phase for each of the surfaces

Latin letters

A	Surface
A_{el}	Surface of the electrode within the EAF
$A_{el\text{-}cool}$	Surface of the electrode, which is wetted from spray cooling
A_i	Surface for view factor calculation
$\vec{A}$	Surface vector
C_p	Heat capacity
d_p	Diameter of dust particles
E_{gas}	Emission of the gas phase
E_i	Emission of the surface i
$\vec{E}$	Emission vector for each of the six surfaces
f	Function of the surface line of the melting cone
G_i	Irradiation of the surface i

$\vec{G}$	Irradiation vector for each of the six surfaces
h	Height
h_{cone}	Cone frustum height in melting geometry
$h_{EAF\ low}$	Bottom EAF vessel height
$h_{EAF\ up}$	Upper EAF vessel height
h_{scrap}	Height of solid scrap
$h_{sSc,0}$	Initial height of charged solid scrap
h_{wall}	Height of the free wall (not covered with solid scrap)
J_i, J_j	Radiosity of the surface i or j
$\vec{J}$	Radiosity vector for each of the six surfaces
K	Constant
$K_{el\text{-}cool\text{-}1}$	Empirical factor for the calculation of the electrode cooling temperature $T_{el\text{-}cool}$
$K_{el\text{-}cool\text{-}2}$	Empirical factor for the calculation of the electrode cooling temperature $T_{el\text{-}cool}$
$K_{el\text{-}rad\text{-}1}$	Empirical factor for the calculation of the electrode radiation temperature $T_{el\text{-}rad}$
$K_{el\text{-}rad\text{-}2}$	Empirical factor for the calculation of the electrode radiation temperature $T_{el\text{-}rad}$
$K_{\alpha\text{-}H2O+CO2,j}$	Correction factor for the calculation of $\alpha_{H2O+CO2,j}$
$K_{\varepsilon\text{-}H2O+CO2}$	Correction factor for the calculation of $\varepsilon_{H2O+CO2}$
$K_{\varepsilon\text{-}H2O\text{-}1,2,3,4}$	Empirical factors for the calculation of ε_{H2O}
$K_{\varepsilon\text{-}CO2\text{-}1,2,3,4}$	Empirical factors for the calculation of ε_{CO2}
L	Length
L_{max}	Maximum length of electrode
m	Mass
m_{el}	Mass of the electrode
M	Molar mass
M	Matrix according to Eq. (21)

p	Pressure
p_i	Partial pressure of element i (with $i =$ CO_2, H_2O)
$p_{i-\alpha,j}$	Partial pressure of element i (with $i =$ CO_2, H_2O) for surface j
P	Power
P_{arc}	Power of electric arc
P_{el}	Electrical Power in electrode
$\dot{Q}$	Heat flow
$\dot{Q}_{el}$	Heat flow from/to the electrode
$\dot{Q}_{el-rad}$	Heat transfer from/to the electrode through radiation
$\dot{Q}_{el-conv}$	Heat transfer from/to the electrode through convection
$\dot{Q}_{el-cool}$	Heat flow from the electrode due to electrode spray cooling
$\dot{Q}_{joule}$	Heat generation within electrode due to P_{el}
$\vec{\dot{Q}}_{rad}$	Heat radiation vector for each of the six surfaces
r	Radius
$r_{cone\ in}$	Inner cone frustum radius
$r_{cone\ out}$	Outer cone frustum radius
$r_{EAF\ in}$	EAF vessel radius at the bottom
$r_{EAF\ out}$	EAF vessel radius at the roof
R_1	Substitution for a better overview within the view factor calculation in Eq. (13)
R_2	Substitution for a better overview within the view factor calculation in Eq. (13)
s_{eq}	Equivalent layer thickness
t	Time
t_{tap}	Tap-to-tap time
T_{el-hom}	Homogeneous electrode temperature
T_{el-rad}	Electrode temperature for radiation heat transfer from/to the electrode $\dot{Q}_{el-rad}$

$T_{el\text{-}conv}$	Electrode temperature for convection heat transfer from/to the electrode $\dot{Q}_{el-conv}$
$T_{el\text{-}cool}$	Electrode temperature for heat transfer due to electrode spray cooling $\dot{Q}_{el-cool}$
T_{gas}	Temperature of the gas phase
$T_{H2O\text{-}m}$	Average temperature of water sprayed for cooling on the electrode
$T_{surf,j}$	Temperature of the surface j
V	Volume
$V_{cone\ frustum}$	Volume of the cone frustum of the meting geometry
V_{sSc}	Volume of the solid scrap
VF	View factor matrix
VF_{ij}	View factor from surface i to surface j
y_1, y_2	Boundaries for the integration of the function f

List of subscripts and superscripts

Numerals

1	EAF roof
2	Water-cooled walls
3	Solid scrap
3-1	Circular ring surface of solid scrap
3-2	Lateral surface of cone frustum
3-3	Circular bottom surface of cone frustum
3-4	Circular ring surface of upper end of cone frustum
4	Melt
5	Arc
6	Electrode

Latin letters

·	Flow
⟶	Vector
arc	Electric arc
cone	
cone frustum	Cone frustum from melting geometry
conv	Convection
cool	Cooling
el	Electrode
el-rad	Radiation from/to electrode
el-conv	Convection from/to electrode
el-cool	Electrode spray cooling
i, j	Surfaces (with *i, j* = 1 (roof), 2 (wall), 3 (sSc), 4 (lSc), 5 (arc), 6 (el))
joule	Heat generation due to dissipation
lSc	Liquid scraprad Radiation
sSc	Solid scrap

Abbreviations

AC	Alternating current
cone	Cone frustum
conv	Convection
cool	Cooling
DC	Direct current
EAF	Electric arc furnace
el	Electrode
hom	Homogenous

lSc	Liquid scrap
lSl	Liquid slag
ODE	Ordinary differential equations
rad	Radiation
sim	Simulated
sSc	Solid scrap
sSl	Solid slag
surf	Surface

Figures

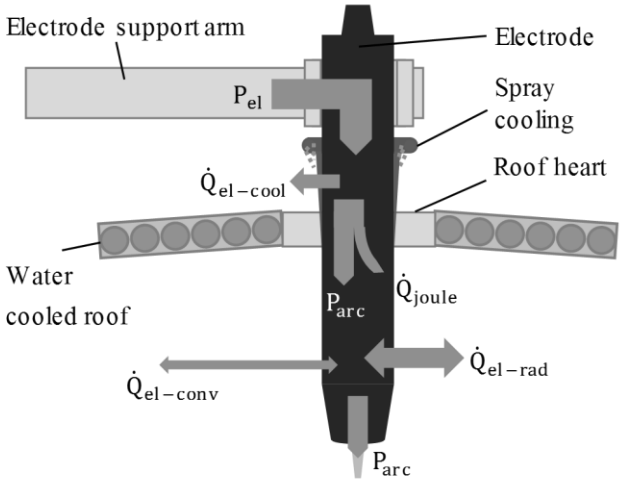

Figure 1. Schematic representation of the electrode energy balance in the EAF model.

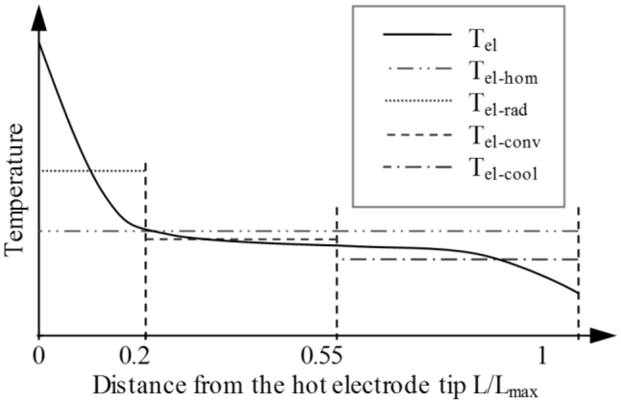

Figure 2. Exemplary temperature profile of the electrode and homogeneous temperatures of selected sections.

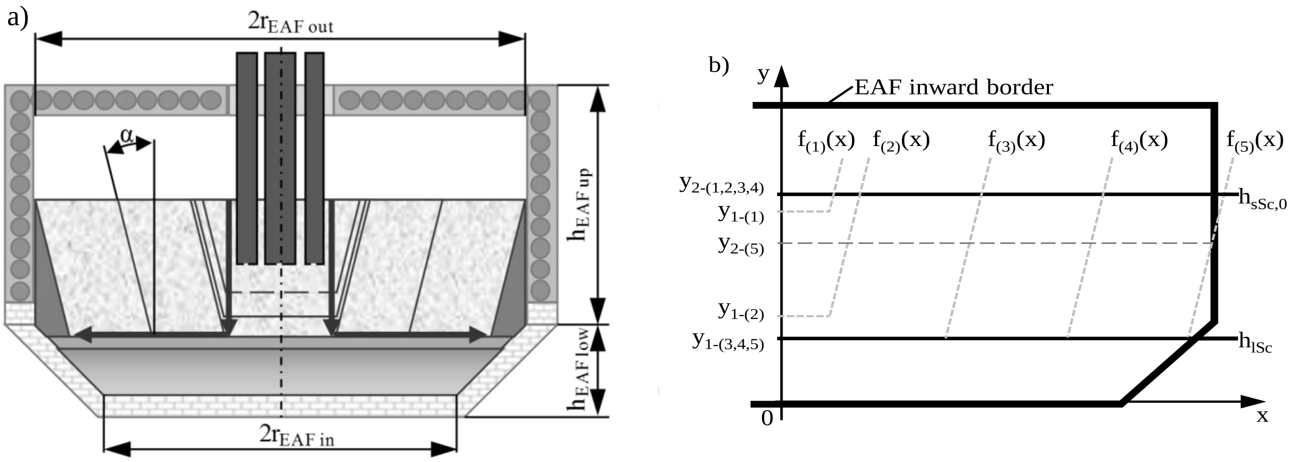

Figure 3. Assumed EAF geometry with assumed spread of the meltdown cone (dark gray arrows) (a); Boundaries of rotation volume (b).

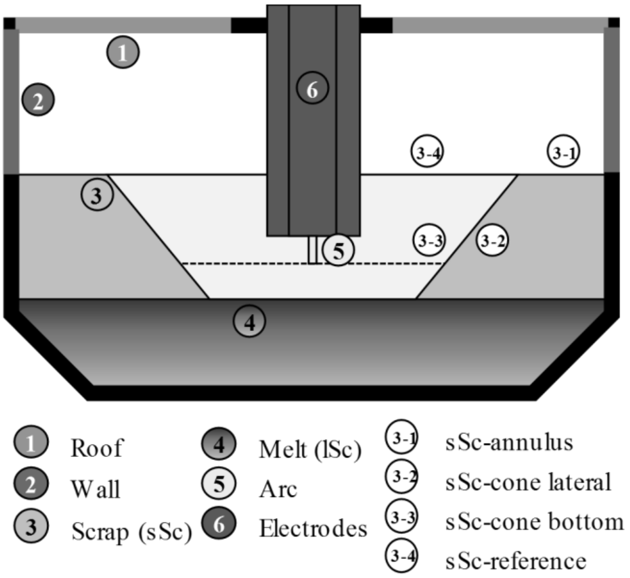

Figure 4. Distribution of the surfaces in the AC-EAF for the calculation of the view factors.

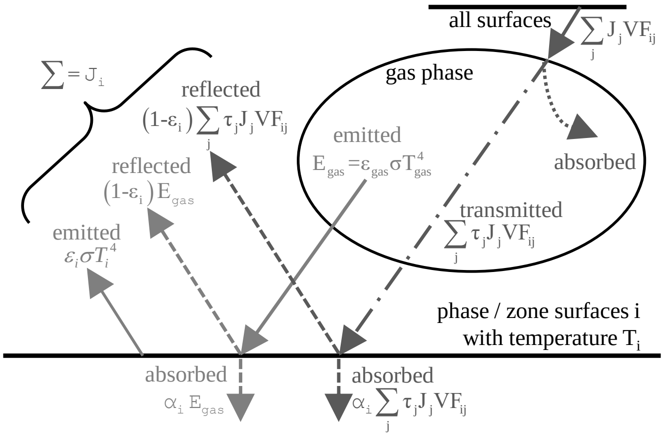

Figure 5. Schematic representation of the thermal radiation.

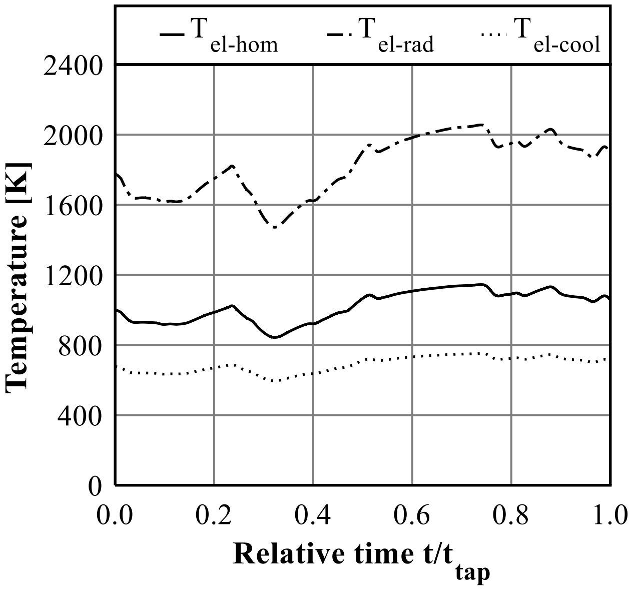

Figure 6. Simulated temperatures of electrode sections.

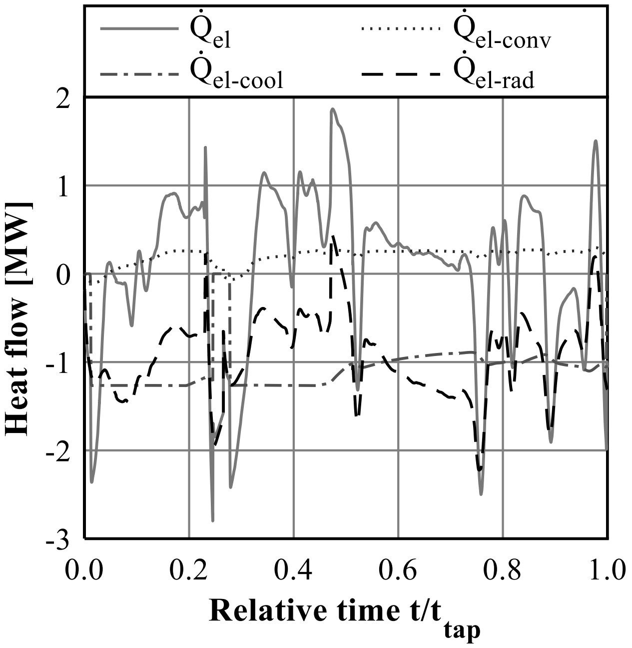

Figure 7. Simulated heat flows of the electrode.

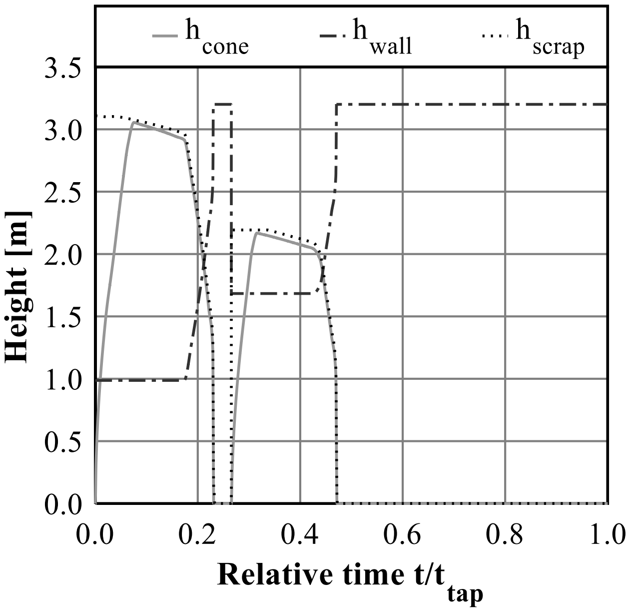

Figure 8. Simulated sizes of the melting geometry: height of the melting cone h_{cone}, the free wall h_{wall} and of the scrap h_{scrap}.

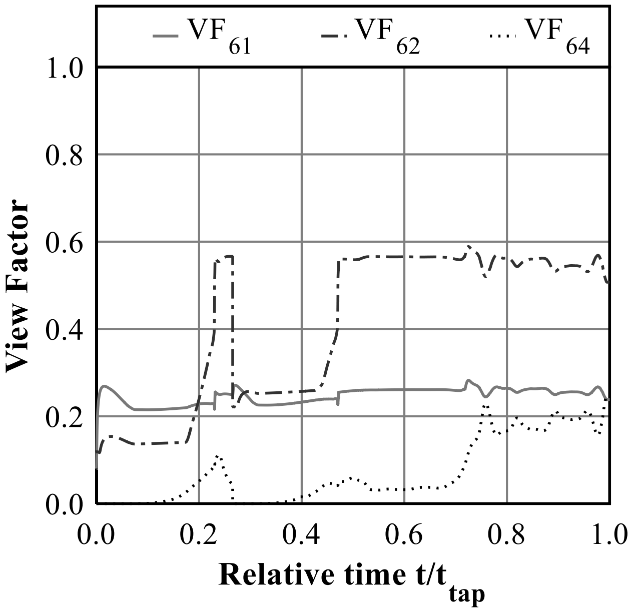

Figure 9. Simulated view factors from electrode (6) to the roof (1) VF_{61}, to the walls (2) VF_{62} and to the melt (4) VF_{64}.

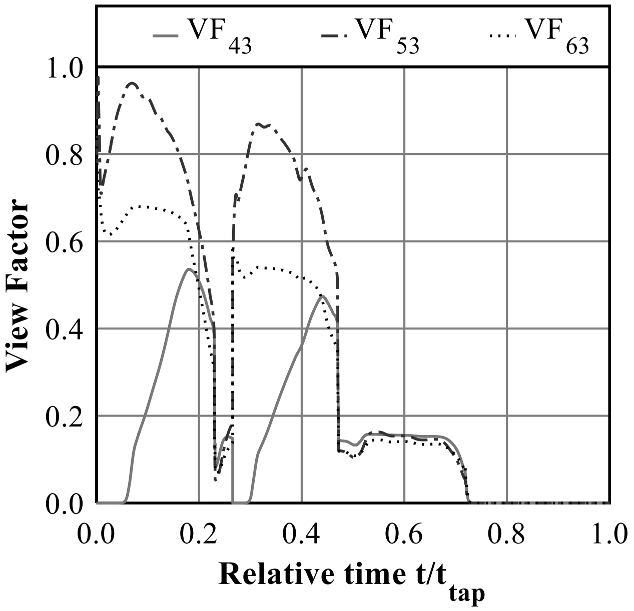

Figure 10. Simulated view factors from the melt (4) VF_{43}, the arc (5) VF_{53} and the electrode (6) VF_{63} to the solid scrap (3).

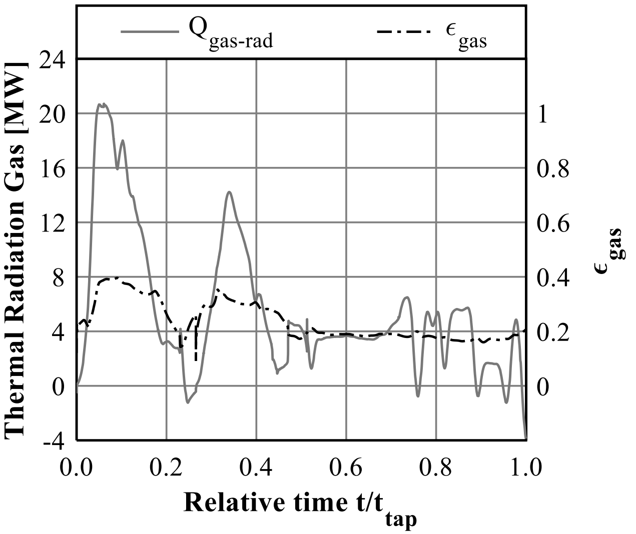

Figure 11. Simulated results for the total gas radiation $\dot{Q}_{gas\text{-}rad}$ and the gas emissivity ε_{gas}.

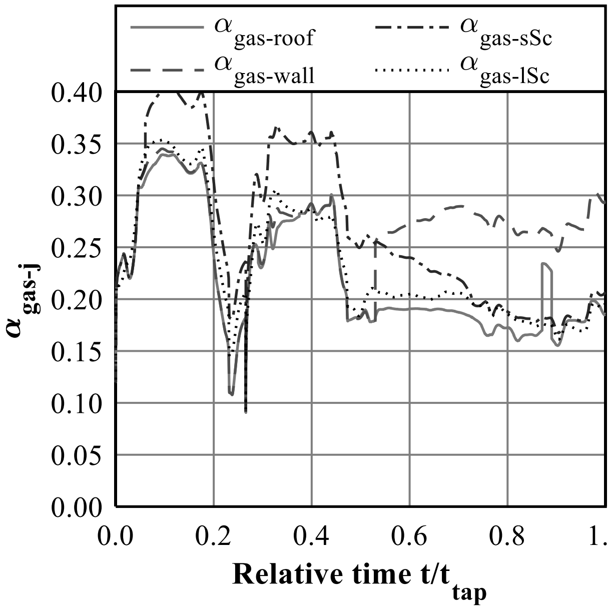

Figure 12. Simulated results for the gas absorptivities for the roof $\alpha_{gas\text{-}roof}$, the wall $\alpha_{gas\text{-}wall}$, the melt $\alpha_{gas\text{-}lSc}$ and the solid scrap $\alpha_{gas\text{-}sSc}$.

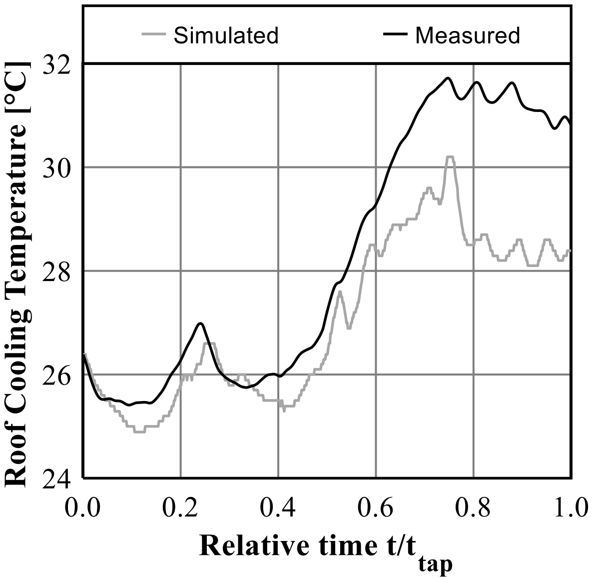

Figure 13. Simulated and measured water temperature at roof cooling outlet

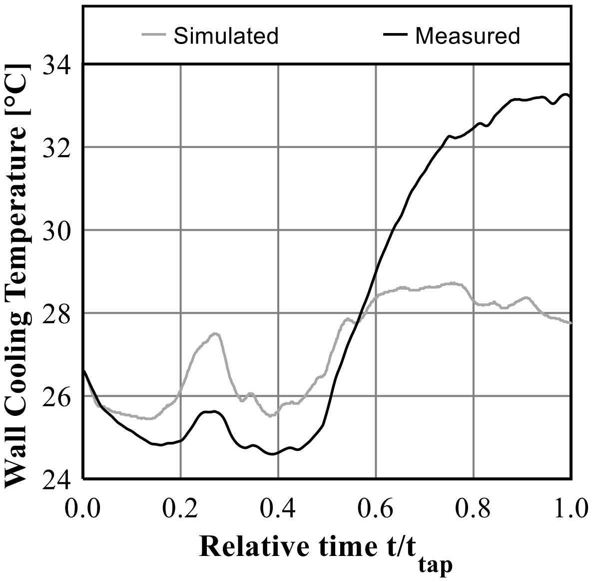

Figure 14. Simulated and measured water temperature at wall cooling outlet

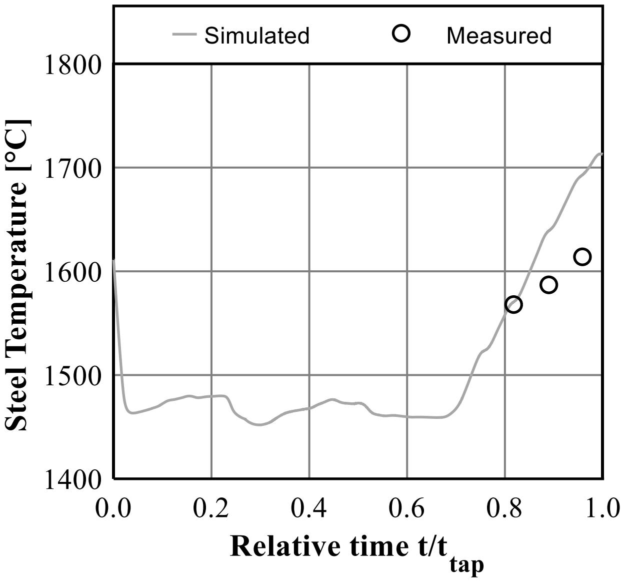

Figure 15. Simulated and measured steel bath temperature

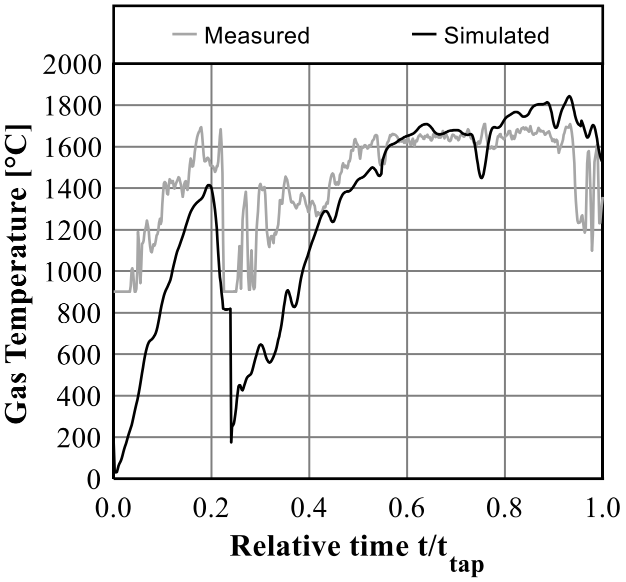

Figure 16. Simulated and measured gas temperature

Tables

Table 1. Empirical factors and correction factors

$K_{el\text{-}rad\text{-}1}$	$K_{el\text{-}rad\text{-}2}$	$K_{el\text{-}cool\text{-}1}$	$K_{el\text{-}cool\text{-}2}$	$K_{\varepsilon\text{-}H2O\text{-}1}$	$K_{\varepsilon\text{-}H2O\text{-}2}$
1.9357	-160.3 K	0.5174	159.4 K	0.747	0.000168

Table 2. Values of parameters used in the model.

$\alpha_{el\text{-}gas}$	r_{el}	$\alpha_{el\text{-}cool}$	$T_{H2O\text{-}m}$	π
0.05 kW m^{-2} K^{-1}	0.355 m	8.5 kW m^{-2} K^{-1}	335.65 K	3.1416
$r_{cone\ in}$	α	$r_{EAF\ in}$	$r_{EAF\ out}$	$h_{EAF\ low}$
0.5 m	60°	2.5 m	3.65 m	1.15 m
$h_{EAF\ up}$	σ	ε_1	ε_2	ε_3
3.2 m	5.67 10^{-8} W m^{-2} K^{-4}	0.3	0.35	0.85
ε_4	ε_5	ε_6	d_p	ρ_{gas}
0.62	1	0.85	500 µm	0
$C_{p,el}$	$K_{slag\_influence}$	$K_{arc\text{-}radiation}$	$K_{arc\text{-}lSc}$	
0.0085 kJ mol^{-1} K^{-1}	0.1	0.6	0.3	